Effect of EVA Encapsulation on Antireflection Properties of Mie Nanoscatterers for c-Si Solar Cells

P. Spinelli, F. Lenzmann, A. Weeber, and A. Polman

Abstract—Dielectric nanoparticle arrays have been proposed as antireflection coatings and light-trapping schemes for thin-film c-Si solar cells. However, practical aspects about the integration of these nanostructures with solar modules have yet to be investigated. In this paper, we study the effect of ethylene vinyl acetate (EVA) encapsulation on the optical properties of dielectric nanoparticles placed on top of c-Si substrates. We experimentally show that Si nanoparticle Mie coatings encapsulated in an EVA layer yield ultralow reflectivity over the entire 300–1000-nm spectral range. The AM1.5-weighted average reflectivity of the Mie coating is as low as 1.5%, which is comparable with that of a standard alkaline texture used for c-Si solar cells. TiO_2 nanoparticle Mie coatings also yield similar results. Mie coatings are thus valid substitutes of standard textures for ultrathin devices. We also study the case of plasmonic nanoparticle coatings for c-Si solar cells. We find that they are not suited for c-Si cells when EVA encapsulation is used.

Index Terms—Light trapping, nanostructures, photovoltaic cells.

I. INTRODUCTION

DIELECTRIC nanoparticles (NPs) have recently been proposed as an antireflection (AR) and light-trapping (LT) scheme for crystalline Si (c-Si) solar cells [1]–[7]. The advantage over standard random pyramid textures commonly used in commercial c-Si solar cells is that dielectric NPs can be applied to solar cells of any thickness, even based on ultrathin ($<5~\mu$m) wafers. Furthermore, dielectric NP coatings also allow decoupling the AR/LT scheme from the surface passivation scheme. In a standard solar cell, a Si_3N_4 layer deposited on the random pyramid texture is used both as an AR coating and as a passivation layer [8], [9]. The increased surface area due to texturing leads to increased surface recombination. Recently, we have shown that an array of TiO_2 nanocylinder placed on top of a flat Al_2O_3-passivated Si surface allows achieving ultralow reflectivity and excellent passivation of the Si surface [10]. Metal NPs have also been proposed as an ARC and LT scheme for c-Si solar cells [11]–[14]. However, the presence of parasitic ohmic

losses in the metal is a strong limiting factor, which makes metal NPs less appealing for application on c-Si solar cells [15].

The physical principle behind the reduced reflectivity by arrays of both dielectric and metallic NP is the preferential forward scattering of light by Mie or plasmonic resonances in the NPs toward the high index substrate [16]. This mechanism works particularly well if the NPs are placed at the interface between c-Si and air, due to the large index mismatch between the two media. However, in commercial modules, c-Si solar cells are never in direct contact with air. In fact, a polymer layer is used to encapsulate the cells in order to protect them from environmental degradation and to achieve mechanical rigidity. Usually, ethylene vinyl acetate (EVA) is used for encapsulation. Glass panels are then added on top of the EVA to add physical stability to the module.

The presence of a polymer layer at the front side of the solar cell changes the optical environment around the resonant NPs and thus their scattering properties. In this paper, we study the effect of EVA encapsulation on the scattering behavior of dielectric NPs. We experimentally test the EVA encapsulation on a Si wafer coated with a Si nanopillar array with the geometry presented earlier for the case without encapsulation in [3]. We report a reflectivity after EVA/glass encapsulation of 5.9%, which includes the reflection of the glass/air interface ($\sim$4.4%). This value is comparable with that of a standard random pyramid texture used on commercial devices. Further optimization carried out with numerical simulation yields even lower reflectivities. TiO_2 NP-based Mie coatings also yield similar results.

II. RESULTS

An array of Si nanopillars that are 250 nm in diameter, 150 nm in height, and have a 450-nm array pitch was fabricated on a 500-μm-thick FZ-Si (1 0 0) wafer by using substrate conformal imprint lithography [17] and reactive ion etching (RIE). The wafer was then coated with a 50-nm-thick Si_3N_4 layer deposited by plasma-enhanced chemical vapor deposition. This configuration is the same presented in [3], which yields an AM1.5-weighted average reflection of 1.3% in the 400–900-nm spectral range, for a Si wafer in air. The wafer with the Si Mie coating was then encapsulated by lamination with a 300-μm-thick EVA sheet, a 3-mm-thick low-iron glass slide at the front, and a white-paint backsheet. Fig. 1(a) shows a schematic of the sample.

Fig. 1(b) shows a photograph of the encapsulated sample. The Si wafer is $\sim 3 \times 2$ cm^2 in size and is embossed into a larger 10×10 cm^2 glass/backsheet frame. The Si wafer with Mie coating looks visually black. Fig. 1(c) shows a scanning electron microscope (SEM) image of a focused ion beam (FIB) prepared cross section of the sample near the front surface, prior
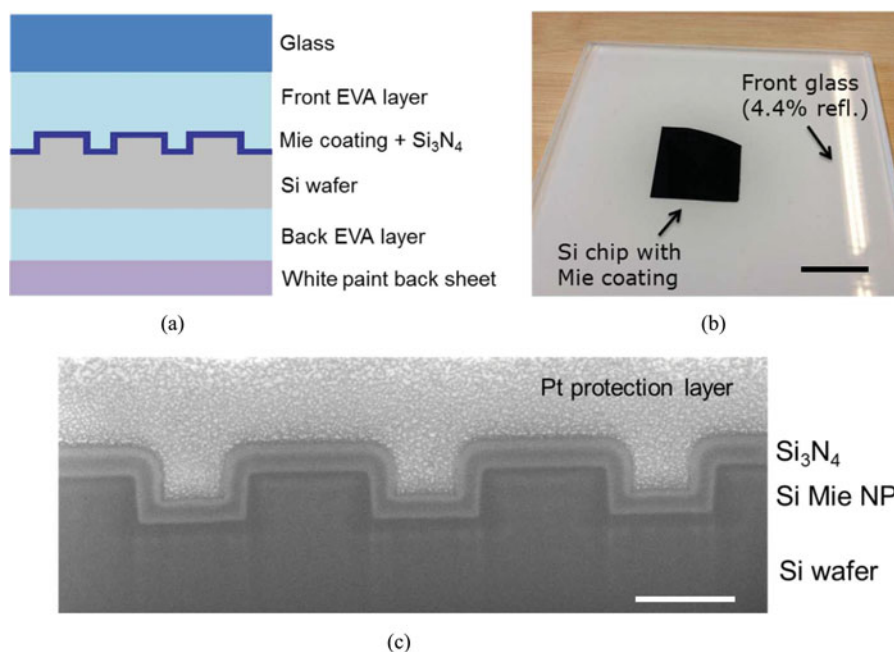
This article has been accepted for inclusion in a future issue of this journal. Content is final as presented, with the exception of pagination.

2

IEEE JOURNAL OF PHOTOVOLTAICS

Fig. 1. (a) Schematic of the sample used for optical characterization (drawing not to scale). (b)Mie-coated Si wafer encapsulated by glass/EVA/white-paint backsheet layers (scale bar represents 2 cm). (c) SEM image of an FIB prepared cross section of the Si Mie coating, comprising Si nanopillars coated by Si_3N_4. The Pt protection layer is also visible. The scale bar represents 200 nm.

to EVA embossing. The Si pillars are clearly visible, showing the excellent anisotropy of the Si RIE. The Si_3N_4 coating is also visible, together with the Pt protection layer used in the cross-sectioning procedure.

Total reflection spectroscopy was used to characterize the samples. An integrating sphere setup equipped with a halogen lamp white-light source (beam diameter of 1.5 cm) and a spectrometer was used. The total reflection of the Mie coating is compared with that of a Si wafer with standard pyramid texture and Si_3N_4 coating. The random pyramids have size varying between 3 and 10 μm, and the Si_3N_4 layer has thickness of $\sim$70 nm and refractive index of $\sim$2.08, which are optimal parameters for textured surfaces.

Fig. 2(a) shows the total reflection as a function of wavelength for an encapsulated Si wafer with the Si Mie coating (red) and for an encapsulated textured Si wafer with standard texture and Si_3N_4 coating (black). The dashed black line represents a constant offset representing the reflection of the top glass layer, which amounts to 4.4% [18]. The reflectivity of the sample with the Mie coating is lower than 5% for a large part of the spectral range. This corresponds to an EVA/Mie-coated Si interface reflection of less than 1% for the entire 500–1100-nm spectral range. The ultralow reflectivity measured in this spectral range is due to the preferential forward scattering of light through leaky Mie resonance in the Si NPs [19], [20]. The reflectivity increases to $\sim$15% for a wavelength of 400 nm, due to backscattered diffraction orders from the grating formed by the NPs (for further details, see the discussion below). An increase of reflectivity is also observed in the IR part of the spectrum (wavelengths above 1020 nm). This is due to the light that escapes from the Si wafer after being reflected by the Si/EVA and EVA/white-paint interfaces at the back.

Overall, the optical performance of the Mie coating embedded in EVA is comparable with that of a standard texture for the 500–1020-nm spectral range. The Mie coating gives higher reflectivity for wavelengths shorter than 500 nm, due to the backscattering from diffraction orders of the grating. This difference can be eliminated by using a random configuration of Mie scatterers. The two reflectivity spectra also differ in the wavelength range above 1020 nm. This is due to a differently textured backside for the standard textured and Mie-coated wafers yielding different LT. A comparison of the LT properties of the two samples is beyond the scope of this paper, which focuses on AR properties, and it will be addressed in future work.

The inset in Fig. 2(a) shows a zoomed view of the reflectivity spectra for the Mie-coated wafer (red) and standard textured wafer (black) in the 400–1000-nm spectral range. The graph shows that the Mie coating yields lower reflectivity than the standard texture in the entire 700–1000-nm spectral range. For both samples, we calculate the average reflectivity by weighting with the AM1.5 global solar spectrum, in the spectral range 300–1000 nm, in order to exclude the LT effects mentioned above from the analysis on AR properties. The Mie coating yields an average reflectivity of 5.9%, compared with an average reflectivity of 5.5% for the standard texture. From these figures, the calculated spectrally averaged EVA/Si interface reflection is 1.5% for the Mie-coated samples, and 1.1% for the standard texture. We conclude that the AR performance of the Mie coating is comparable with that of a standard texture coated with Si_3N_4. Thus, the Mie coating is a valid alternative to standard textures, for example if the thickness of the cell does not allow the use of the latter.

Next, we use finite-difference time-domain (FDTD) simulations to validate the measured data and to find an optimal
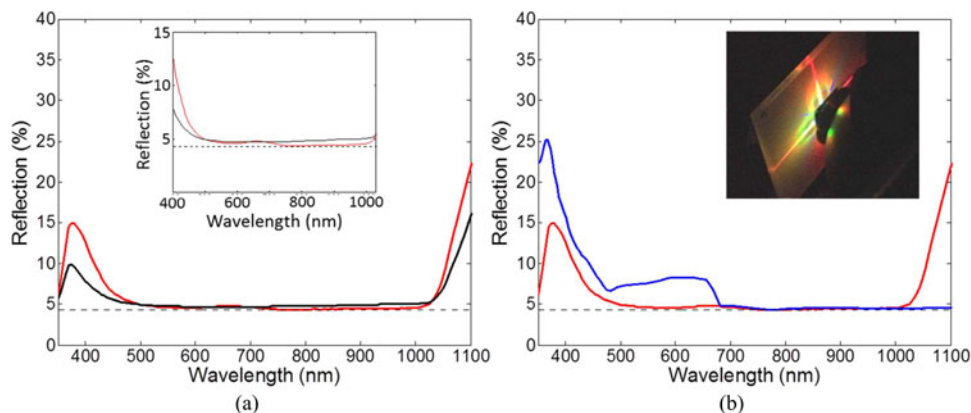
Fig. 2. (a) Measured reflection spectra of an EVA/glass encapsulated Si wafer with Si Mie coating (red) and with standard texture (black). The inset shows a zoomed view of the spectra in the 400–1000-nm spectral range. (b) Simulated (blue) and measured (red) reflection spectra for a Si wafer with Si Mie coating [same data as in (a)]. The inset is a photograph of the sample taken during the measurement, showing the diffraction orders trapped in the glass/EVA layers that are visible due to reflection off the white-paint backsheet.
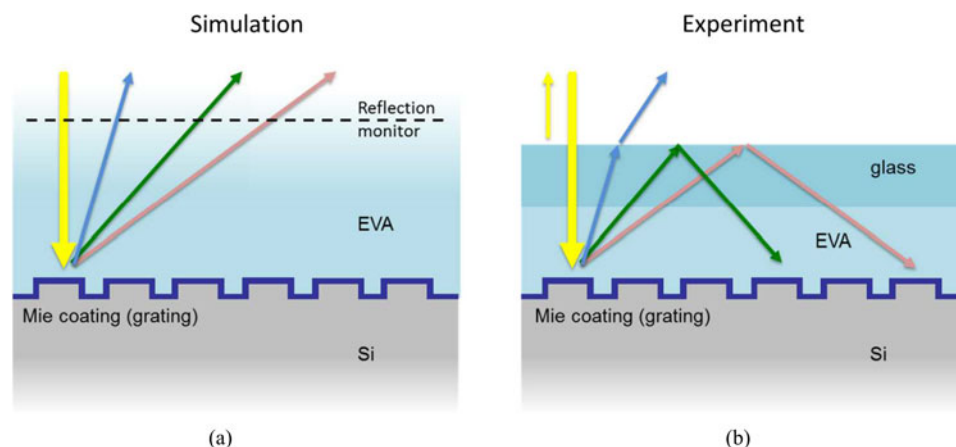

Fig. 3. Schematic of the sample geometry used in the simulation (a) and in the measurement (b). The yellow arrow represents the incident beam, while the colored arrows represent the diffraction orders for different wavelengths.

geometry for the Mie coating embedded in EVA. In order to reduce computational time, we assume an EVA layer that extends semiinfinitely from the wafer surface in the vertical direction. Similarly, we assume a semiinfinite Si substrate, which also extends in the vertical direction. The Mie coating is placed in between the EVA and Si layers (see Fig. 3(a) for a schematic of the simulation setup). Light is incident from the EVA side on the Mie-coated Si substrate, and reflection is calculated with an optical power monitor on the EVA side. To avoid that light is absorbed before reaching the Si surface, we assume that the EVA layer has no absorption.

Fig. 2(b) shows the measured (red) and simulated (blue) reflectivity spectra of the Mie-coated Si wafer. The simulated reflectivity spectrum has been corrected with an offset of +4.4%, in order to account for the air/glass interface reflection (not considered in the simulation; see Fig. 3). Excellent agreement between the measured and simulated data is observed for the wavelength range 670–1020 nm. For wavelengths larger than 1020 nm, the measured reflectivity is larger than the simulated one, due to the backscattered light from the Si/EVA and EVA/white-paint interfaces, which is not accounted for in the

simulations. For wavelength shorter than 670 nm, the simulated reflectivity is larger than the measured one. In order to understand this, Fig. 3 shows two schematics of the sample geometry used in the simulations (a) and experiment (b). In the simulation setup, the backscattered grating orders (colored arrows) all contribute to the reflectivity. The grating order modes set in for wavelengths that satisfy the following condition:

$$\lambda = \sin \theta \frac{np}{m} \qquad (1)$$

where λ is the wavelength, θ is the emission angle of the grating order, n is the refractive index of the medium (in this case EVA, $n = \sim 1.5$), p is the grating pitch, and m is the integer describing the grating order. For an array pitch of 450 nm, as the one considered here, (1) has solutions only if $\lambda < 670$ nm. Therefore, the sharp increase in the simulated reflectivity spectrum occurring at a wavelength of 670 nm [see the blue line in Fig. 2(b)] is due to the onset of backscattered grating orders.

In the experiment, however, the EVA layer has a finite thickness and is capped by a 3-mm glass layer. Thus, grating orders that are scattered at an angle larger than the critical angle of
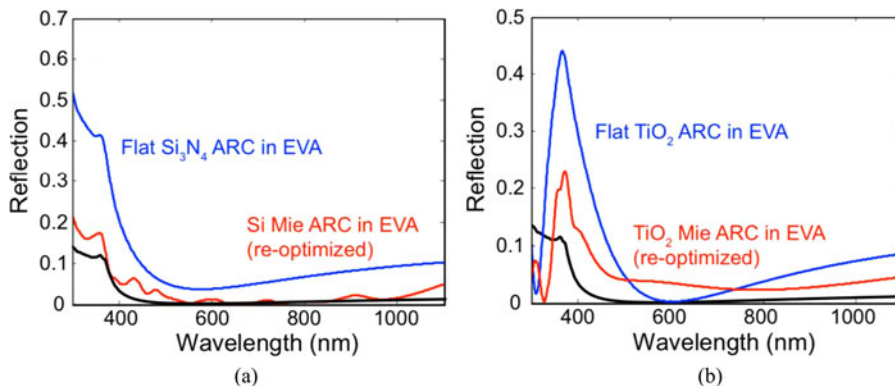
This article has been accepted for inclusion in a future issue of this journal. Content is final as presented, with the exception of pagination.

4   IEEE JOURNAL OF PHOTOVOLTAICS

Fig. 4. (a) Simulated reflection spectra for a Si Mie coating (red) and a flat Si_3N_4 ARC (blue), both embedded in EVA. (b) Simulated reflection spectra for a TiO_2 Mie coating (red) and a flat TiO_2 ARC (blue), both embedded in EVA.
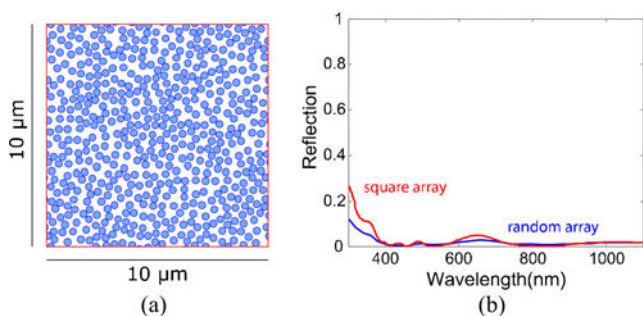

Fig. 5. (a) Schematic of a random array of Mie scatterers used in the simulations. (b) Comparison between the reflectivity of a random (blue) and periodic (red) array of Mie scatterers.

glass/air interface will undergo total internal reflection and be redirected toward the Si substrate [see Fig. 3(b)]. Light in these grating orders is then mostly transmitted into the Si layer via scattering of Mie resonances in the NPs at the surface. This explains why the measured reflectivity in Fig. 2(b) is lower than the simulated one. Note that the EVA layer has a refractive index which very closely matches that of glass ($n = {\sim}1.5$); therefore, only minor reflections occur at the EVA/glass interface. For very short wavelengths [see the blue arrow in Fig. 3(b)], the diffraction angle is smaller than the critical angle of the glass/air interface, and thus, light will escape from the sample. This explains the increase in reflectivity observed in the measurements for wavelengths below 500 nm.

The presence of backscattered grating orders that undergo total internal reflection at the glass/air interface was directly observed during the experiment. The inset in Fig. 2(b) shows a photograph of the sample under illumination. Several colored lines can be seen in specific directions, aligned with the grating formed by the NPs. These lines are grating orders that are redirected toward the surface by total internal reflection, and they are visible to the eye by scattering off the white-paint backsheet surrounding the Si chip. On a large-area solar cell, this light would be absorbed in the cell. As already mentioned, the presence of grating orders can be avoided by employing a random configuration of Mie scatterers (see Fig. 5).

The geometry considered in the experiment described above was optimized for the case of a Si wafer in direct contact to air. We use FDTD simulation to find an optimal geometry of the Mie coating for the case of an EVA-encapsulated Si substrate. The simulation layout is the same as sketched in Fig. 3(a). We use a particle swarm algorithm to find the optimal geometry. Note that due to the simplified geometry considered in the simulations (see Fig. 3), the optimal geometry of the simulated system may differ from that of a real system.

Fig. 4(a) shows the simulated reflectivity spectra for an optimized Si NP Mie coating (red) and a flat 80-nm-thick Si_3N_4 layer (blue). The reflectivity of standard random pyramid textures coated with a 70-nm-thick Si_3N_4 layer is also shown for reference (black). The latter has been calculated using the OPAL2 optical simulator software [21].

The optimized Si Mie coating yields ultralow reflectivity over the entire 400–1000-nm spectral range. The sharp increase in reflectivity for wavelengths below 400 nm is due to backscattered grating orders. As observed before, in a real device, the actual reflectivity in this spectral range will be lower. Thus, from the simulated data, we can calculate the upper limit for the AM1.5-averaged reflectivity over the 300–1100-nm spectral range. For the Si Mie ARC in EVA, it is 2.1%, compared with an average reflection of 9% for the flat Si_3N_4 coating and of 1.3% for the standard texture. The found optimal geometry for the Si Mie coating in EVA is 210-nm particle diameter, 260-nm particle height, 345-nm array pitch, and 65-nm Si_3N_4 coating.

Fig. 4(b) shows the results for the case of a TiO_2 NP-based Mie coating, similar to the one in [10]. The simulated reflection spectrum for the TiO_2 Mie coating is shown in red, and it is compared with that of a flat 65-nm-thick TiO_2 ARC (blue) and of a standard Si_3N_4-coated texture (black). In addition, in this case, the Mie coating yields lower reflectivity than a flat dielectric coating. The AM1.5-weighted average reflectivity for the TiO_2 Mie coating is less than 4.2%, while the average reflectivity of the flat TiO_2 coating is 6.4%. Note that some parasitic absorption is present in the TiO_2 NPs. However, this is limited to the spectral range below 400 nm [10], where EVA also shows parasitic absorption of light. Therefore, in a solar module, the optical losses in the TiO_2 Mie coating are mitigated by the presence of optical losses in the EVA encapsulation.
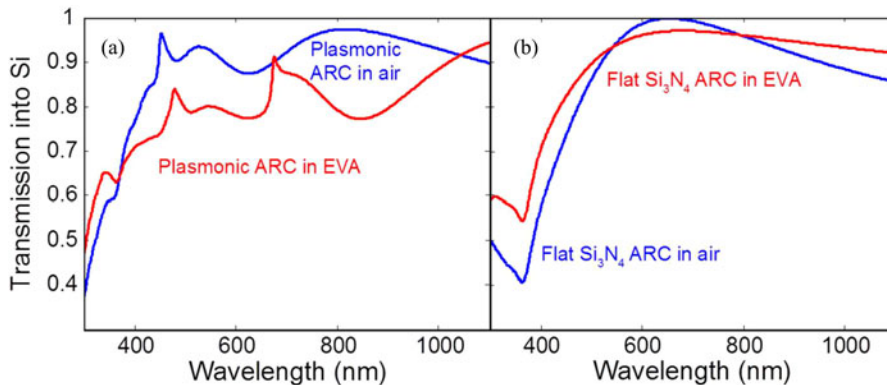
Fig. 6. (a) Simulated reflection spectra for a plasmonic Ag coating in air (blue) and in EVA (red). (b) Simulated reflection spectra for a flat Si_3N_4 ARC in air (blue) and EVA (red).

The simulated optimal geometry in this case is 120-nm particle diameter, 80-nm particle height, and 200-nm array pitch on top of a 65-nm-thick TiO_2 layer. Interestingly, we note that a flat TiO_2 ARC gives lower reflectivity than a flat Si_3N_4 ARC when EVA is considered. This is due to the fact that almost perfect impedance matching is achieved at a wavelength of 600 nm, where $n_{TiO_2} = \sqrt{n_{Si}n_{EVA}}$.

Overall, Fig. 4 shows that both the Si NP Mie coating and the TiO_2 NP Mie coating are valid substitutes of the Si_3N_4-coated standard texture for ARC when an EVA encapsulation is used. Mie coatings, however, have the advantage that they can be applied to ultrathin wafers. Furthermore, the TiO_2 Mie coating can be applied to a flat passivated Si surfaces. Thus, despite its lower optical performance compared with a standard texture, the TiO_2 Mie coating allows for a reduced surface recombination compared with a textured cell, due to the lower surface area.

As a last remark, we note that while diffraction gratings have been widely studied as a way to reduce reflection for Si devices [22], [23], the main mechanism behind the reduction of the reflectivity by arrays of dielectric NPs is the scattering of light by Mie resonances in single NPs. Fig. 5 (b) shows the simulated reflectivity spectra of an array of Si Mie NPs on a Si wafer, arranged in a periodic (red) and aperiodic (blue) arrays. Fig. 5(a) shows the simulation geometry used in the simulations.

As can be seen, both the periodic and aperiodic array of Mie nanoscatterers yield very low reflectivities for the entire range 300–1100 nm. They both show a reflection minimum at a wavelength of 850 nm, which corresponds to the first-order Mie resonance of the Si NPs. Interestingly, the random configuration shows even a lower reflectivity than the periodic array in the spectral range 300–400 nm, due to the lack of backscattered grating order. Overall, Fig. 5 proves that the main mechanism behind the reduction in reflectivity is scattering from Mie resonances in single NPs. Grating effects are also present for periodic configurations, but they play a minor role in reducing the reflection (in fact, they may play a detrimental role by creating diffraction orders that are backscattered to air or EVA, as shown in Fig. 3).

Finally, we consider the case of arrays of plasmonic (Ag) NPs. We have shown before that plasmonic coatings yield better AR properties than a flat Si_3N_4 coating [24]. It is thus interesting

to study how plasmonic coatings perform when an EVA encapsulation is used. For this analysis, we use FDTD simulations to calculate the transmission into a Si substrate covered with an array of spheroidal Ag NPs with optimal geometry (from [24]: 180-nm diameter, 130-nm height, and 450-nm pitch, on top of a 50-nm-thick Si_3N_4 spacer layer).

Fig. 6(a) shows the simulated transmission into the Si substrate as a function of wavelength, for the plasmonic coating in air (blue) and in EVA (red). Simulations were done using a semiinfinite EVA layer thickness, similar to the case of the dielectric Mie coating presented above.

The plasmonic coating in air shows transmission larger than 90% for the entire 450–1100-nm spectral range. We note two main features in the transmission spectrum: a sharp feature at a wavelength of 450 nm and a broad S-shaped feature in the range 600–800 nm. The first is due to the Rayleigh anomaly of the $[\pm1, 0]$ and $[0, \pm1]$ grating orders of the grating formed by the Ag NPs and occurs at a wavelength equal to the array pitch [25]. Note that for wavelengths below 450 nm, the transmission drops due to backscattering of grating orders (see the discussion about Figs. 2(b) and 3). The S-shaped feature at $\sim$700 nm is due to Fano interference, i.e., the destructive and constructive interference between scattered and incident waves occurring for wavelengths below and above the particle localized surface plasmon resonance (LSPR) wavelength [24], [26]. When the Ag NP array is embedded in EVA (red line), both features redshift. The Rayleigh anomaly of the $[\pm1, 0]$ and $[0, \pm1]$ grating orders redshifts to a wavelength of 675 nm due to the increase of the surrounding medium refractive index from 1 to 1.5. A second Rayleigh anomaly, corresponding to the $[\pm1, \pm1]$ grating orders, appears at a wavelength of $\sim$480 nm.

The Fano line shape also redshifts to a wavelength of $\sim$1000 nm when the EVA encapsulation is applied. This is also a direct consequence of the large redshift of the LSPR when the particle is embedded in a higher index medium [19]. Both effects drastically reduce the transmission of light into the Si substrate for the 300–1100-nm spectral range. The average transmission, weighted with the AM1.5 solar spectrum, drops from 91% to 80.7%. For comparison, Fig. 6(b) shows the transmission spectra of a flat 80-nm-thick Si_3N_4 ARC in air (blue) and EVA (red). The average transmission for a flat Si_3N_4 ARC in air and for

the EVA covered ARC is 89.4% and 91.3%, respectively. Thus, while the plasmonic coating works better for light coupling than a standard flat Si_3N_4 ARC in air, the opposite is true when an EVA encapsulation is applied.

In our analysis, we varied particle size and array pitch, and we found that none of the geometry considered yields better transmission than a flat Si_3N_4 coating. The results of this parameter optimization show that the highest transmission is obtained for largest pitch considered (1 μm) and the smallest NP size considered (40-nm diameter). Even in this configuration, the transmission into the Si was lower than that of a flat Si_3N_4 coating (let alone of a textured Si_3N_4-coated surface). This suggests that the optimization procedure was leading to a configuration where the particles are more and more spaced from each other, and smaller and smaller—which eventually leads to having no NPs at all. The simulations thus suggest that it is very difficult to obtain excellent antireflective properties, like those of dielectric NP coatings, with Ag plasmonic coatings when EVA is used for encapsulation.

Note that this result is valid within the simulation parameter space studied (Ag NPs with 40–200-nm diameter, arranged in arrays of 200–1000-nm pitch). Other plasmonic nanostructure configurations can lead to beneficial effects for solar cells. For example, metal nanowire networks can be used to combine high transmission of light with excellent electrical conductivity [27]. Thus, they can be used to replace unwanted ITO films. Furthermore, plasmonic nanostructures made of Al may be better than Ag nanostructures due to a more blue-shifted LSPR of Al with respect to Ag [28].

III. Conclusion

We have studied the effect of EVA encapsulation on the AR properties of dielectric NPs placed on top of c-Si substrates. We experimentally showed that Si NP Mie coating encapsulated in an EVA layer yields ultralow reflectivity over the entire 300–1000-nm spectral range. The AM1.5-weighted average reflectivity of the Mie coating is less than 2.1%, and it is thus comparable with that of a standard alkaline texture used for c-Si solar cells. TiO_2 NP-based Mie coatings also yield similar results. Mie coatings are thus a valid alternative to standard textures for ultrathin devices. We find that plasmonic coating is instead not suited for use in c-Si solar cells when an EVA encapsulant is used.

Acknowledgment

References

[1] M. Brongersma, Y. Cui, and S. Fan, "Light management for photovoltaics using high-index nanostructures," *Nature Mater.*, vol. 13, pp. 451–460, 2014.

[2] A. Polman and H. A. Atwater, "Photonic design principles for ultrahigh-efficiency photovoltaics," *Nature Mater.*, vol. 11, pp. 174–177, 2012.

[3] P. Spinelli, M. A. Verschuuren, and A. Polman, "Broadband omnidirectional antireflection coating using subwavelength surface Mie resonators," *Nature Commun.*, vol. 3, pp. 692-1–692-5, 2012.

[4] E. Massa *et al.*, "Diffractive interference design using front and rear surface metal and dielectric nanoparticle arrays for photocurrent enhancement in thin crystalline silicon solar cells," *ACS Photon.*, vol. 1, pp. 871–877, 2014.

[5] J. Eisenlohr *et al.*, "Hexagonal sphere gratings for enhanced light trapping in crystalline silicon solar cells," *Opt. Exp.*, vol. 22, pp. A111–A119, 2014.

[6] P. Spinelli and A. Polman, "Light trapping in thin crystalline Si solar cells using surface Mie scatterers," *IEEE J. Photovoltaics*, vol. 4, no. 2, pp. 554–559, Mar. 2014.

[7] M. van Lare, F. Lenzmann, and A. Polman, "Dielectric back scattering patterns for light trapping in thin-film Si solar cells," *Opt. Exp.*, vol. 21, pp. 20738–20746, 2013.

[8] M. A. Green, *Solar Cells: Operating Principles, Technology and System Applications*. Sydney, Australia: Univ. New South Wales, 1998.

[9] W. H. Southwell, "Pyramid-array surface-relief structures producing antireflection index matching on optical surfaces," *J. Opt. Soc. Amer.*, vol. 8, pp. 549–553, 1991.

[10] P. Spinelli *et al.*, "Al_2O_3/TiO_2 nano-pattern antireflection coating with ultralow surface recombination," *Appl. Phys. Lett.*, vol. 102, pp. 233902-1–233902-4, 2013.

[11] H. A. Atwater and A. Polman, "Plasmonics for improved photovoltaic devices," *Nat. Mater.*, vol. 9, pp. 205–213, 2010.

[12] P. Matheu *et al.*, "Metal and dielectric nanoparticle scattering for improved optical absorption in photovoltaic devices," *Appl. Phys. Lett.*, vol. 93, pp. 113108-1–113108-3, 2008.

[13] S. Pillai *et al.*, "Surface plasmon enhanced silicon solar cells," *J. Appl. Phys.*, vol. 101, pp. 93105-1–93105-3, 2007.

[14] T. L. Temple *et al.*, "Influence of localized surface plasmon excitation in silver nanoparticles on the performance of silicon solar cells," *Sol. Energy Mater. Sol. Cells*, vol. 93, pp. 1978–1985, 2009.

[15] P. Spinelli and A. Polman, "Prospects of near-field plasmonic absorption enhancement in semiconductor materials using embedded Ag nanoparticles," *Opt. Exp.*, vol. 20, pp. 641–654, 2012.

[16] K. R. Catchpole and A. Polman, "Design principles for particle plasmon enhanced solar cells," *Appl. Phys. Lett.*, vol. 93, pp. 191113-1–191113-3, 2008.

[17] M. A. Verschuuren and H. van Sprang, "3D photonic structures by sol-gel imprint lithography," *Mater. Res. Soc. Symp. Proc.*, vol. 1002, pp. N03-1–N03-6, 2007.

[18] (2013). [Online]. Available: http://www.glasolutions.ch/switzerland/images/fck/diamant_solar.pdf

[19] G. Mie, "Beitrage zur Optik truber Medien, speziell kolloidaler Metallosungen," *Ann. Phys.*, vol. 330, pp. 377–445, 1908.

[20] J. van de Groep and A. Polman, "Designing dielectric resonators on substrates: Combining magnetic and electric resonances," *Opt. Exp.*, vol. 21, pp. 26285–26302, 2013.

[21] K. R. McIntosh and S. C. Baker-Finch, "OPAL 2: Rapid optical simulation of silicon solar cells," presented at the 38th IEEE Photovoltaic Spec. Conf., Austin, TX, USA, 2012.

[22] M. G. Moharam, *Holographic Optics: Design and Applications*. Bellingham, WA, USA: SPIE, 1988, pp. 8–11.

[23] C. Heine and R. H. Morf, "Submicrometer gratings for solar energy applications," *Appl. Opt.*, vol. 34, pp. 2476–2482, 1995.

[24] P. Spinelli *et al.*, "Optical impedance matching using coupled metal nanoparticle arrays," *Nano Lett.*, vol. 11, pp. 1760–1765, 2011.

[25] J. W. S. Rayleigh, "Note on the remarkable case of diffraction spectra discovered by Prof. Wood," *Philosophical Mag.*, vol. 14, pp. 60–65, 1907.

[26] B. Luk'yanchuk *et al.*, "The Fano resonance in plasmonic nanostructures and metamaterials," *Nature Mater.*, vol. 9, pp. 707–715, 2010.

[27] J. van de Groep, P. Spinelli, and A. Polman, "Transparent conductive silver nanowire networks," *Nano Lett.*, vol. 12, pp. 3138–3144, 2012.

[28] N. P. Hylton *et al.*, "Loss mitigation in plasmonic solar cells: Aluminium nanoparticles for broadband photocurrent enhancements in GaAs photodiodes," *Sci. Rep.*, vol. 3, pp. 2045–2322, 2013.

Authors' photographs and biographies not available at the time of publication.